Mitochondrial protein interactome elucidated by chemical cross-linking mass spectrometry

Devin K. Schweppe[a,1], Juan D. Chavez[a,1], Chi Fung Lee[b,c,d], Arianne Caudal[b,c,d], Shane E. Kruse[e], Rudy Stuppard[e], David J. Marcinek[e], Gerald S. Shadel[f,g], Rong Tian[b,c,d], and James E. Bruce[a,2]

[a]Department of Genome Sciences, University of Washington, Seattle, WA 98105; [b]Department of Bioengineering, University of Washington, Seattle, WA 98105; [c]Department of Anesthesiology and Pain Medicine, University of Washington, Seattle, WA 98105; [d]Mitochondria and Metabolism Center, University of Washington, Seattle WA 98105; [e]Department of Radiology, University of Washington, Seattle, WA 98105; [f]Department of Pathology Yale School of Medicine, New Haven, CT 06510; and [g]Department of Genetics, Yale School of Medicine, New Haven, CT 06510

Edited by F. Ulrich Hartl, Max Planck Institute of Biochemistry, Martinsried, Germany, and approved December 28, 2016 (received for review October 17, 2016)

Mitochondrial protein interactions and complexes facilitate mitochondrial function. These complexes range from simple dimers to the respirasome supercomplex consisting of oxidative phosphorylation complexes I, III, and IV. To improve understanding of mitochondrial function, we used chemical cross-linking mass spectrometry to identify 2,427 cross-linked peptide pairs from 327 mitochondrial proteins in whole, respiring murine mitochondria. In situ interactions were observed in proteins throughout the electron transport chain membrane complexes, ATP synthase, and the mitochondrial contact site and cristae organizing system (MICOS) complex. Cross-linked sites showed excellent agreement with empirical protein structures and delivered complementary constraints for in silico protein docking. These data established direct physical evidence of the assembly of the complex I–III respirasome and enabled prediction of in situ interfacial regions of the complexes. Finally, we established a database and tools to harness the cross-linked interactions we observed as molecular probes, allowing quantification of conformation-dependent protein interfaces and dynamic protein complex assembly.

mitochondria | mass spectrometry | interactome | cross-linking | protein interaction reporter

Mitochondrial proteins play a diverse role in cellular biology and disease. Mitochondrial dysfunction directly causes multiple inherited diseases (1) and is implicated in common diseases, including neurological developmental disorders (2, 3), neurodegenerative and cardiovascular diseases (4–6), diabetes (7), asthma (8), cancer (9), and age-related disease (10). In mammals, these organelles have evolved to retain more than 1,000 proteins that interact within a complex, i.e., dual membrane architecture (11, 12). Within the mitochondrial proteome, the "powerhouse" functions are carried out by the core constituents of the oxidative phosphorylation (OXPHOS) system [complexes I–IV of the electron transport chain (ETC) and ATP synthase (complex V)]. These proteins are necessary for creation of the mitochondrial electrochemical gradient that powers synthesis of ATP. This system includes critical protein–protein interactions within individual OXPHOS complexes as well as "supercomplex" interactions between ETC complexes I, III, and IV in the respirasome (13). Deficient supercomplex formation has been proposed as a critical mitochondrial defect in failing hearts (5, 6, 14, 15), and dynamic rearrangement of supercomplexes has been implicated in noncanonical mitochondrial functions such as antibacterial innate immune responses (16). Assessing these interactions is further complicated by regulatory posttranslational modification and conformational changes of mitochondrial proteins (17–20). Advances in this area have been impeded, in part, by the lack of large-scale detection of dynamic, sometimes transient, interactions between membrane proteins. Thus, large-scale determination of the protein interactome within mitochondria would provide a valuable tool to advance understanding of mitochondrial function and dysfunction and would provide a strong complement to new cryo-EM–derived structures of mitochondrial complexes (21).

Chemical cross-linking mass spectrometry (XL-MS) capabilities now have developed to enable high-throughput identification of protein interactions in complex mixtures and living cells (22, 23). Work by many groups has led to improvements in instrumentation (24), cross-linker chemistry (25, 26), database searching (23, 24, 27, 28), spectral match filtering (29), and structural analysis based on sites of cross-linking (30–32). Large-scale XL-MS offers two key benefits. First, in conjunction with *in silico* modeling of structures, the identification of cross-linked interactions enables the observation of the physical features of proteins, including membrane proteins (33, 34). These capabilities can uncover novel functions derived from protein–protein interactions, and cross-links have provided data complementary to cryo-EM and crystallography to enhance the understanding of the structure and function of complex systems (27). Second, large-scale chemical cross-linking analyses applied to living systems can enable the determination of protein interactions and conformational changes in complex, dynamic native environments, including the quantification of changes in response to pharmacological intervention (35). In the present study protein interaction reporter (PIR)-based XL-MS was performed using a peptide-based chemical cross-linking molecule for unambiguous identification of cross-linked peptides (33, 34, 36–38). PIR workflows leverage tandem mass spectrometry (MS^n, where n = stages of MS) methods based on the expected PIR mass relationships observed between MS and

Significance

Mitochondria meet the majority of living cells' demand for ATP and, as important regulators of redox homeostasis, metabolite levels, and calcium buffering, are a critical link between cell energetics and signaling. Disruption of these processes can induce adaptive or pathological signaling responses to stress and under severe stress promote cell death. Mitochondria have a complex proteome with conformations and interactions that are not well understood. Mitochondrial dysfunction is a direct cause of rare inherited diseases and is implicated in common metabolic diseases and age-related pathology. This study illuminates protein interactions and conformational features of nearly one-third of the mitochondrial proteome. Network information on this scale will enable groundbreaking insights into mitochondrial function, dysfunction, and potential therapeutic targets for mitochondrial-based pathology.

Author contributions: J.D.C., D.J.M., G.S.S., R.T., and J.E.B. designed research; D.K.S., J.D.C., C.F.L., A.C., S.E.K., and R.S. performed research; D.K.S. and J.D.C. analyzed data; and D.K.S., J.D.C., C.F.L., D.J.M., G.S.S., R.T., and J.E.B. wrote the paper.

The authors declare no conflict of interest.

This article is a PNAS Direct Submission.

[1]D.K.S. and J.D.C. contributed equally to this work.

[2]To whom correspondence should be addressed. Email: jimbruce@uw.edu.

This article contains supporting information online at www.pnas.org/lookup/suppl/doi:10.1073/pnas.1617220114/-/DCSupplemental.

MS^2 spectra to enable spectral identification of peptides and protein–protein interactions (24).

We applied PIR technologies to determine protein interactions in functional mitochondria and identified 2,427 nonredundant cross-linked peptide pairs from 327 mitochondrial proteins across 459 protein–protein interactions. These data provide insight into the structures of many mitochondrial proteins, including the five OXPHOS complexes. Importantly, intercomplex cross-linked peptides were identified, supporting the existence of respirasomes in whole, respiring mitochondria. These data enable structural modeling of large protein assemblies in situ, in excellent agreement with cryo-EM models. In the future, identified in situ cross-linked sites can be used as molecular probes for the study of condition-specific protein complex formation and conformations and the roles of these complexes in mitochondrial function, dysfunction, and disease.

Results and Discussion

Chemical cross-linking provides evidence of proximal solvent-accessible sites on proteins in vivo and is a means to predict and assemble models of protein structures (34, 35, 39). It is important to note that the chemical cross-linking workflow in this study was performed on whole, functional mitochondria. The resulting cross-links provide evidence for protein interactions in their native environment because respiring mitochondria were harvested and cross-linked to ensure the capture of physiologically relevant in situ interactions (Fig. 1*A*) (17, 40). The activity of isolated cardiac mitochondria was examined by substrate-driven respiration (Fig. 1*B*). Mitochondria were loaded with pyruvate and malate as substrates, and oxygen consumption rates (OCR) were measured after the addition of ADP and then oligomycin A. The addition of ADP induced robust oxygen consumption (state 3 respiration), whereas the addition of the ATP synthase/complex V inhibitor oligomycin A lowered the OCR (state 4 respiration). Isolated cardiac mitochondria from the same protocol showed efficient calcium uptake (41). The high respiratory control ratio (RCR = 11.7, the ratio of state 3/state 4 OCR) indicates that the isolated mitochondria were highly coupled (42). Therefore these mitochondria contained functional OXPHOS complexes and intact inner mitochondrial membranes.

Functional, respiring mitochondria were cross-linked in situ using a PIR cross-linker, biotin-aspartate proline-PIR n-hydroxyphthalimide (BDP-NHP) (33–35, 39), and were assembled into an interactome consisting of 2,427 nonredundant cross-linked peptide pairs across 11 individual murine samples (Dataset S1). We identified 327 unique mitochondrial proteins, 31.3% of the murine mitochondrial proteome (327 of 1,042 proteins; MitoCarta 2.0) (Fig. 1*C*) (43), a greater than fourfold increase over recent studies identifying protein interactions in the mitochondrial interactome (44).

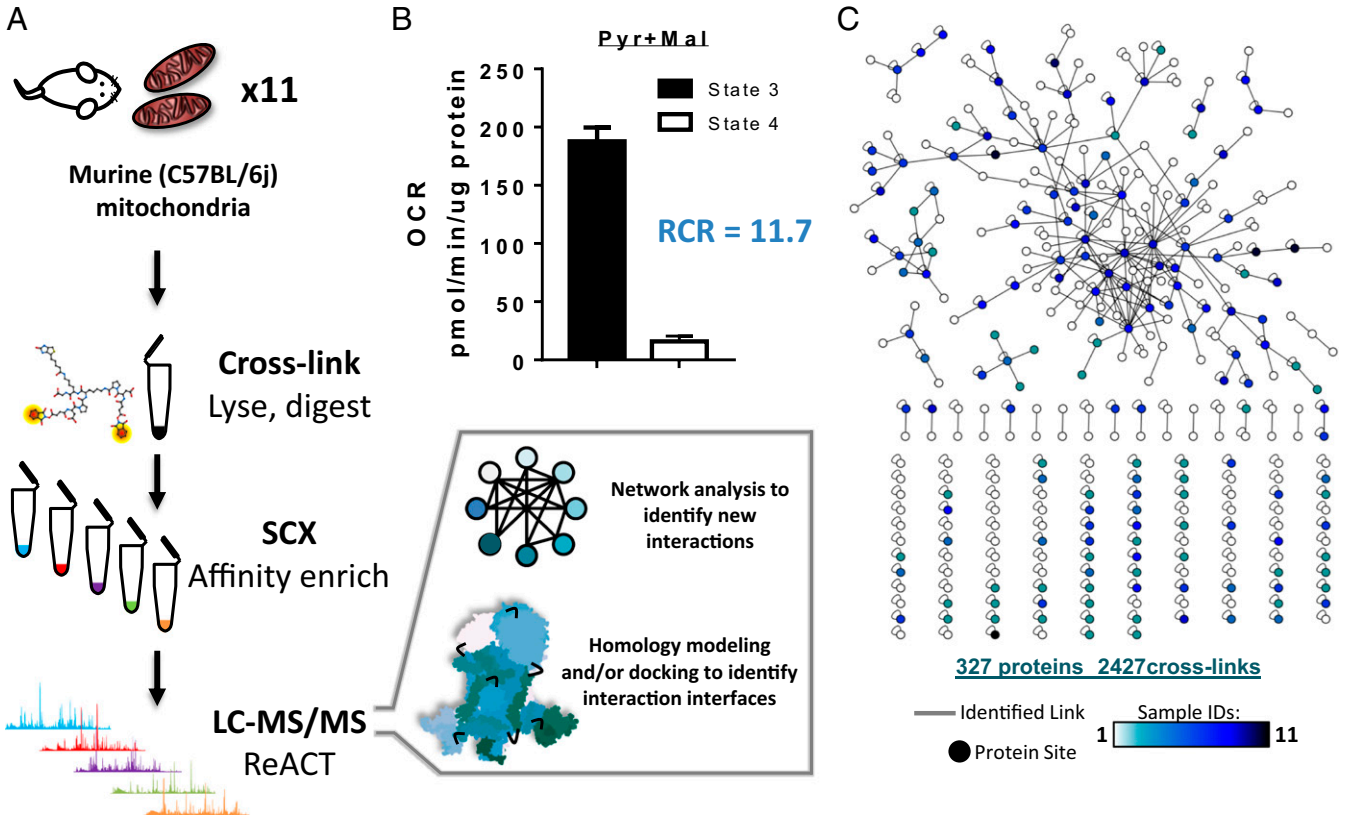

Fig. 1. Determination of cross-linked protein interactions in functional mouse mitochondria. (*A*) Functional mitochondria were cross-linked and lysed, and protein lysates were digested with trypsin, followed by SCX fractionation on the cross-linked peptides. Pooled SCX fractions were enriched with monomeric avidin to capture the biotin-containing cross-linker covalently bound to two peptides. Cross-linked peptides were identified by MS/MS and ReACT (24). (*B*) The OCR of isolated mitochondria with pyruvate and malate as substrates was measured. After the baseline measurements, 50 μL of 40-mM ADP (4 mM final concentration) and 55 μL of 25 μg/mL oligomycin A (2.5 μg/mL final concentration), a complex V inhibitor, were injected sequentially. The changes in OCR after the addition of ADP (state 3) and then oligomycin A (state 4) were measured by Seahorse XF24. The RCR is expressed as state 3 OCR/state 4 OCR. Data were expressed as the SD from five technical replicates. (*C*) Protein interactions as determined by large-scale chemical cross-linking analysis of functional mouse heart mitochondria. Nodes represent individual proteins; edges (lines) represent all cross-links identified between two proteins. Nodes are colored according to the number of samples in which each protein interaction was observed. An interactive network depicting site-to-site interactions is available in Dataset S2.

We note that acetylation previously has been shown to be an important modification in functional mitochondria (17). Therefore we included the modification while searching our LC-MS^n data. We were able to identify many peptides that were both cross-linked and acetylated (Dataset S1). An example was an acetylated lysine residue within the ATP/ADP translocase protein ADT1 at K52. This acetylation event was coidentified within a cross-linked peptide pair linking ADT1 K49 to K147. Homologous sites from a bovine empirical structure of ADT1 [Protein Data Bank (PDB) ID code 2C3E] are depicted in Fig. S1*A* (45). This link highlighted the potential of identifying posttranslational modifications within large-scale cross-linking datasets and points to the future use of XL-MS to dissect the roles of posttranslational modifications and their effects on protein interactions.

A total of 571 nonredundant cross-linked interactions were mapped to the large, multisubunit mitochondrial contact site and cristae organizing system (MICOS) and OXPHOS complexes. The MICOS/mitochondrial intermembrane space-bridging (MIB) proteins are critical for normal inner membrane morphology and cristae formation (46). However, little information was available for the MICOS complex, a subcomplex of the MIB complex. We identified eight cross-linked MICOS/MIB complex proteins that demonstrate site-specific interactions in the MICOS/MIB complex (Fig. S1*B*) (47), including MIC19 and MIC60 homo-multimerization (in which the same lysine site is linked to itself) (Fig. S1 *B* and *C*), as well as cross-links between MIC60's C terminus and three MICOS proteins (MIC10, MIC13, and MIC19) (Fig. S1 *C* and *D*).

Six cross-linked sites in MIC60 (K281 and K639) and MIC19 (K77, K86, K121, and K136) were cross-linked to themselves (e.g., a peptide containing K281 was linked to a second peptide containing K281), suggesting that at least part of the MICOS complex multimerizes, potentially aligning as ATP synthase multimers during the establishment of cristae morphology (47). These findings were supported by previously reported MIC60 dimer, trimer, and tetramer formation (48) and suggested that two regions in the intermembrane space domain of MIC60 (around K281 and K639) were involved in multimer formation (Fig. S1*D*). Site-specific mapping of cross-linked interactions on MIC60 identified three MICOS proteins (MIC10, MIC13, and MIC19) binding close to the C terminus of MIC60 (amino acids 639–725) (Fig. S1*D*), a region known to be required for crista junction formation (49). MIC19, in particular, was observed in three nonredundant links to the MIC60 C terminus (to MIC60 K498, K515, and K639) (Fig. S1*D*). These findings establish putative binding interfaces within MIC60 that enable the protein to act as a scaffold for the MICOS complex in general. We also identified a link between MIC60 and the dynamin-like protein optic atrophy 1 (Opa1), MIC60 K119 to Opa1 K710 (Fig. S1*D*), that identifies an interfacial region for these proteins near the N terminus (K119) of MIC60. As a final point, we observed interactions between the MICOS/MIB complex protein MIC27 and subunits ATPA, ATP5F1, and ATP5J of the F_1 domain of ATP synthase, including two ATP synthase stator domain proteins, ATP5F1 and ATP5J (50, 51). These ATP synthase interactions with MICOS/MIB provide structural insight (stator binding) consistent with the reported roles of MICOS/MIB complexes in coordinating with OXPHOS complexes, including ATP synthase, to define the architecture of the inner mitochondrial membrane.

OXPHOS complexes (complexes I–IV and ATP synthase) are critical for ATP production in mitochondria. We observed cross-links within the OXPHOS complexes that showed excellent agreement with previous structural data (Fig. S2). These included a homo-multimeric link between two molecules of QCR2 with K159 observed linked to itself (K159–K159) with a Cα–Cα distance of 22.8 Å (murine QCR2 was overlaid on a yeast complex III dimer structure), well within the empirically derived maximum linkable distance (35 Å) of BDP-NHP (24, 35, 52, 53) (Fig. 2*A* and Fig. S3*A*). We further compared cross-links against the empirical structures for OXPHOS complexes II and IV as well as electron transport flavoproteins ETFA and ETFB (Fig. 2 *B*–*D*) based on conserved lysine residues in the empirical structures. In each of these examples we observed the Cα–Cα distances between cross-linked lysines to be less than 35 Å (Fig. 2).

Extending in situ analysis to another OXPHOS complex, we mapped cross-linked lysine sites across ATP synthase (complex V). We identified cross-linked residues within each of the major extramembrane domains of the complex: rotor, stator, and ATPA/B (Fig. S2). We further observed that 13% (41 of 318) of cross-linked relationships within ATP synthase were between ATPA/B and the stator (Fig. 2*E*). These cross-links provide distance constraints to refine molecular interactions between ATP synthase subunits and information on the relationship between ATP8 and other complex V subunits (Fig. 2*E*). It has been proposed that ATP8 serves a fundamental role in the assembly and/or production of ATP by F-ATPases (54). XL-MS (54) and cryo-EM (55) studies on ATP synthase complexes purified from bovine and *Pichia angusta*, respectively, indicate that ATP8 interacts with subunits of the stator, providing structural stability to the peripheral stalk. The structure of ATP8 is predicted to consist of a short N-terminal domain exposed in the intermembrane space (IMS) followed by a transmembrane helix and a flexible, disordered C-terminal tail that extends up from the membrane into the mitochondrial matrix. In purified bovine ATP synthase, two sites were previously identified as linking residues K46 and K54 of ATP8 to subunits b (AT5F1), d (ATP5H), and F_6 (ATP5J) in the stator (K120, K24, and K73 respectively) (54). We identified four cross-linked residues in ATP8 (K46, K48, K54, and K57) linked to six other ATP synthase subunits, including the stator subunits ATP5H (subunit d: K25, K85, K95, K117, K148, and K149), ATP5J (subunit F_6: K99 and K105), and AT5F1 (subunit b: K162), the rotor subunits ATPD (K136) and ATP5E (K50), and the core subunit ATPA (K498) (Fig. 2*E* and Fig. S4). Furthermore, mapping of a homology model of ATP8 to cryo-EM–derived structures of ATP synthase in multiple rotational states (55) revealed that links between ATP8 (K46 and K48) and the rotor subunit ATPD (K136) are possible only with ATP synthase rotational state 3. In contrast, the link between ATP8 (K48) and the rotor subunit ATP5E (K50) was possible only in rotational state 1 (Fig. 2*E*). These cross-links confirmed existing XL-MS data obtained from purified bovine ATP synthase in murine ATP synthase from functional mitochondria (54) and established interactions within the rotor and core subunits that are rotational-state dependent.

We also observed cross-linked interactions between the ATP synthase inhibitor ATIF1 and the F_1 domain proteins ATPA and ATPB (Fig. S5). Using a full-length model of the murine ATIF1 structure, we docked the inhibitor to an empirical ATP synthase F_1-domain structure containing ATIF1 protein fragments (PDB ID code: 4Z1M) (56). Three of five links between ATIF1 and ATPA/B were well within the cross-linker Cα–Cα distance threshold (ATPA–ATIF1: 25.8 Å; ATPB–ATIF1: 13.8 Å and 29.7 Å). However, the predicted ATIF1 model contained an extended C-terminal α-helix not present in the empirical structure (Fig. S5). When the extended helix was overlaid on protein fragments from the empirical structure, we observed two cross-links between the C terminus of ATIF1 and ATP synthase subunit ATPB with Cα–Cα distances greater than 50 Å, longer than the BDP-NHP linker. The long Cα–Cα distances suggested that the ATIF1 C-terminal α-helix may have a flexible conformation that would not be visible by X-ray crystallography but would allow binding to the external surface of ATPB and could be arrested by chemical cross-linking (Fig. S5). Identification of potentially dynamic or transient interactions are particularly interesting, because it was established previously that cross-linked peptide abundances change in a conformation-dependent

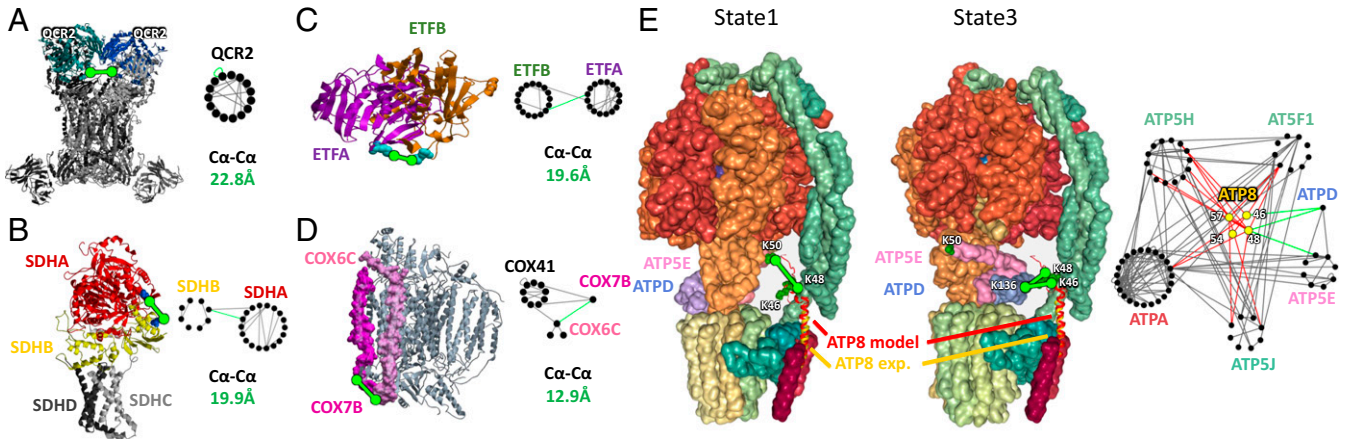

Fig. 2. Cross-linked sites mapped to empirical protein structures. Sites of cross-linking identified in empirical structures are shown along with site–site interaction networks. Cross-links are depicted as space-filled residues and green lines. Cα–Cα distances for the links are shown. Network nodes represent individual cross-linked sites; edges represent identified cross-links. Cross-links highlighted in each structure are shown as green edges in the network (78). (*A*) Complex III dimer (monomers shown in light gray and dark gray). Homology model of mouse QCR2 overlaid on the yeast complex III structure (PDB ID code: 1KYO). The mouse QCR2 proteins for monomers one and two are shown in blue and teal, respectively. (*B*) Homology models of mouse SDHA and SDHB were overlaid on the porcine complex II structure (PDB ID code: 4YXD) (79). Identified cross-linked lysines are highlighted in blue. (*C*) The ETFA–ETFB complex structure (PDB ID code: 1EFV) (78) from human, with conserved lysine sites highlighted in teal. Mouse ETFA (purple) K139 corresponds to human K139, and mouse ETFB (orange) K26 corresponds to human R26. (*D*) Complex IV structure from bovine with COX7B (magenta) and COX6C (pink) highlighted (PDB ID code: 3ASO) (80). Mouse COX7B K75 (corresponding to bovine K51) and mouse COX6C K68 (corresponding to bovine K65) link the proteins on the IMS side of the complex. (*E*) The Phyre2 model of ATP8 (red) was superimposed on a helix assigned to ATP8 (yellow) in cryo-EM–derived structures (55) of ATP synthase in rotational state 3 (PDB ID code: 5LQX) and rotational state 1 (PDB ID code: 5LQZ). Cross-linked sites (green space-filled residues) between APT8 (K46 and K48) and ATPD (K136) are compatible with state 3, whereas the cross-link between ATP8 (K48) and ATP5E (K50) is compatible only with state 1. Cross-linked sites involving ATP8 and six other ATP synthase subunits are indicated in the subnetwork and are displayed on a structure in Fig. S4.

manner (35); thus future studies could harness the ATIF1–ATPA/B links to elucidate condition- and conformation-specific flexing of the ATIF1 helix.

Building on such dynamic complex interactions, we observed multiple intercomplex links between respirasome supercomplex components complex I and complex III that facilitated cross-link distance-constrained rigid body docking. Even before they were mapped to the docked model, these cross-links provided evidence of the assembly of an OXPHOS supercomplex within whole, functional mitochondria. The resulting docked model of the complex I [PDB ID code: 5LDW (57)]–complex III [PDB ID code: 1KYO (58)] supercomplex (Fig. 3) (59) indicated that both complex III monomers interact simultaneously with complex I: QCR2 from one complex III monomer and QCR6 from the second complex III monomer interacted with complex I's NDUA2 (in the matrix) and NDUB4 (in the intermembrane space), respectively (Fig. 3*A* and Fig. S6).

We compared the XL-MS–based supercomplex model with a recently published ovine cryo-EM structure (PDB ID code: 5J8K) (21). We note that the XL-MS–based supercomplex was assembled without prior knowledge of the cryo-EM structure. Strikingly, after blind assembly of the supercomplex, the final in situ XL-MS model strongly agreed with the cryo-EM structure for complex I and complex III (rmsd = 1.3 Å and 2.4 Å, respectively). We did not observe links between complex III and complex IV, as is consistent with studies that showed these two complexes do not coimmunoprecipitate from Black-6 murine mitochondria, such as those used here, because of a mutation in the scaffolding protein SCAF1 (60). The in situ cross-linked peptides from whole, respiring mitochondria presented here establish a final conformation of complex I–complex III that is highly similar to the cryo-EM model and a set of powerful molecular probes that can be used in the future to quantify conditional response on supercomplex assembly in functional mitochondria (35).

Furthermore, we identified cross-linked sites between subunits of complex I and ATP synthase of the OXPHOS system (Fig. S2). As discussed in a recent review (61), supercomplexes between ATP synthase and complexes of the respiratory chain are known to form, but there are conflicting reports on the association of

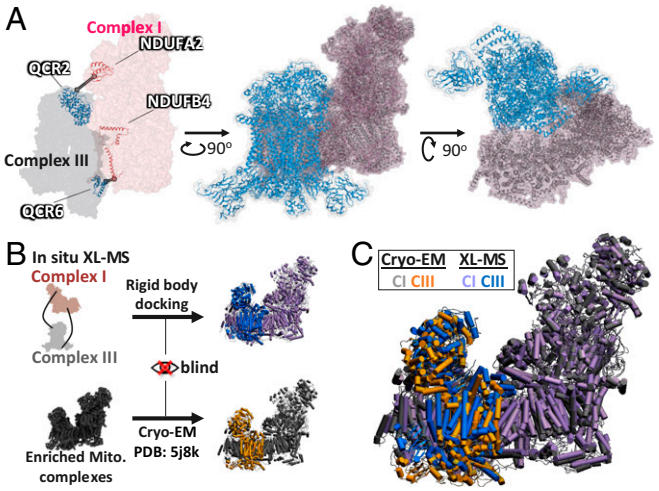

Fig. 3. Determination of supercomplex structures from functional mitochondria. (*A*) Supercomplex model from rigid body docking (59) of complex I (NDUA2, NDUA4) and complex III (QCR2, QCR6) using cross-linked peptide distance constraints (NDUA2–QCR2; NDUA4–QCR6). Complex I is shown in pink, and complex III is shown in blue. Ribbon models of intercomplex cross-linked proteins are shown within the surface model in the left panel, and the distance constraints used are displayed as gray lines. (*B*) Workflow for the comparison of a recently published cryo-EM structure (PDB ID code: 5J8K) (21) and the XL-MS–based supercomplex model. The XL-MS–based model was generated without prior knowledge of the cryo-EM model. (*C*) Comparison of the in situ XL-MS docked supercomplex with the cryo-EM supercomplex model (PDB ID code: 5J8K). Structures were aligned based on complex I. Complex I rmsd = 1.3 Å; complex III rmsd = 2.4 Å.

SYSTEMS BIOLOGY

complex I and complex V (62–64). The links identified between complexes I and V support the existence of this interaction in respiring mitochondria, but the structural implications of these cross-links will require further study taking into account the role of cristae formation and large mitochondrial membrane topologies. Current structural knowledge of complex I places NDUA8 and NDUS5 on the IMS face of the complex, opposite the mitochondrial matrix where the ATP synthase components ATPO, ATB, and ATF5 reside in fully assembled complexes. However, it is not yet known when these links form or if this interaction occurs only during certain stages of complex assembly. Nonetheless, the links identified here provide valuable evidence that could be used to probe the interactions of either the subassemblies of the complexes or the fully assembled complex I and complex V. These links could help shed light on the hypothesis that ATP synthase dimers form the mitochondrial permeability transition pore (mPTP) (65) and the relationship between complex I activity and the mPTP (66–69).

The work presented in this paper focused on a small subset of interaction models that can be derived from cross-linked peptides, including those identified between ATP8, ATIF1, and ATP synthase components, the MICOS complex, and between subunits of complexes I and III. These links highlight a few of the more than 2,400 cross-linked peptide pairs presented in this work. However, the full dataset also includes preliminary findings for other protein complexes such as interprotein interaction interfaces involving the mitochondrial RNA polymerase POLRMT. Previous work has shown that, in addition to a direct role in mitochondrial transcription, POLRMT is involved in mitochondrial translation and ribosome biogenesis (70). In the current study we identified cross-linked sites between murine POLRMT and the mitochondrial translation initiation factor IF-2 that are consistent with these proposed secondary functions (70). Last, each of the cross-linked peptide pairs identified here has the potential to serve as a molecular probe for the future study of dynamic in vivo protein conformations and interactions (35, 71).

To allow rapid, simple dissemination of these data for future studies, we developed tools to allow non–XL-MS experts to take advantage of the mitochondrial interactome data presented here. First, we generated two databases to enable (*i*) targeted quantitative analysis of protein–protein relationships by parallel reaction monitoring (PRM) (71) and (*ii*) large-scale identification of new datasets by spectral matching (Fig. S7) (27, 72). Importantly, neither PRM nor spectral library matching requires specialized instrumentation to identify and quantify XL-MS interactions, so these techniques can be transferred rapidly between laboratories and core facilities (71), allowing wide dissemination of XL-MS–based analysis of mitochondrial proteins. Second, to enable widespread use of these data by the community, we developed a flexible web tool (github.com/mammmals/crosslink-PRMtransitionForm) (71) to allow users to generate PRM transitions for any cross-linked peptide interaction identified in this study using any user-selected cross-linker or desired modification.

The work presented here highlights the utility of in situ XL-MS to determine protein interactions in complex, native conditions. These data are complementary to current structural biology techniques and offer several key benefits for the research community. First, this interactome provides evidence for mitochondrial protein interactions and complex interfaces that should be of high value to the community in general (e.g., MICOS/MIB site interactions). Second, the interactome provides evidence for the presence and orientation of OXPHOS supercomplexes from intact, respiring mitochondria. Finally, the identified cross-linked peptides will enable future studies to target and quantify protein and complex conformational changes, including site-specific perturbation of interaction interfaces, in situ.

Methods

Mitochondrial Isolation Protocol. In total, 11 murine mitochondrial biological replicates were isolated from four mouse tissues [heart, brain, liver, and skeletal muscle (leg)] as previously described (40, 73). See *SI Methods* for details.

Mitochondrial Respiration Using Seahorse XF24 Analyzer. The OCR of isolated cardiac mitochondria was measured with a XF24 Extracellular Flux Analyzer (Seahorse Bioscience) according to the manufacturer's protocol. See *SI Methods* for details.

Synthesis of the BDP-NHP Cross-Linker. The mass spectrometrically cleavable cross-linker BDP-NHP was synthesized as described previously (24). See *SI Methods* for details.

Cross-Linking of Mitochondria and Preparation for LC-MS/MS/MS. Purified mitochondria were resuspended in cross-linking buffer (170 mM Na_2PO_4, pH 8.0) and were cross-linked with 5 mM BDP-NHP for 30 min at room temperature. The mitochondria were lysed, and proteins were extracted and digested with trypsin. Digested peptides were desalted with a C18 Sep-Pak cartridge (Waters), followed by strong cation exchange (SCX) fractionation and enrichment with monomeric avidin (Ultralink; Pierce). See *SI Methods* for details.

LC-MS/MS/MS, Real-Time Analysis of Cross-Linked Peptide Technology, and Data Analysis. Samples were resuspended in 5% (vol/vol) acetonitrile (ACN)/2% (vol/vol) formic acid and were injected in technical duplicate into an in-house–pulled 45-cm C8 (Reprosil, 5-μm, 120-Å) column protected by a 2-cm C8 trapping column. Cross-linked peptides were identified using real-time analysis of cross-linked peptide technology (ReACT)-based instrument methods (24). See *SI Methods* for details. Released peptide spectra (precursors in MS^2, fragments in MS^3) were searched against a target-decoy database constructed from the MitoCarta 2.0 database of annotated mitochondrial proteins from mice (43) using Comet (74). See *SI Methods* for details.

The peptide spectral match false-discovery rate (FDR) was filtered to be less than 5% based on PeptideProphet e-value scoring (24, 75). See *SI Methods* for details. Protein–protein interaction (PPI) networks were displayed using Cytoscape. The large-scale network of mitochondrial interactions will be available on XLinkDB 2.0 (53). A fully interactive version of the network from Fig. 1 is available in Dataset S2.

A spectral library was generated using the cross-linked identifications observed in this study, as described previously (29). This spectral library is available in Dataset S3.

Structure Prediction, Protein Modeling, and Protein–Protein Docking. Structure prediction was performed using Phyre2 (76). Docking of protein complexes was performed with PatchDock (59). Structures were displayed using ICM Brower Pro (MolSoft) or NGL Viewer (77). See *SI Methods* for details. Modeled structures are available in Dataset S4.

1. Wallace DC (2005) A mitochondrial paradigm of metabolic and degenerative diseases, aging, and cancer: A dawn for evolutionary medicine. *Annu Rev Genet* 39:359–407.
2. Anitha A, et al. (2012) Brain region-specific altered expression and association of mitochondria-related genes in autism. *Mol Autism* 3(1):12.
3. Waldbaum S, Patel M (2010) Mitochondria, oxidative stress, and temporal lobe epilepsy. *Epilepsy Res* 88(1):23–45.
4. Lionaki E, Markaki M, Palikaras K, Tavernarakis N (2015) Mitochondria, autophagy and age-associated neurodegenerative diseases: New insights into a complex interplay. *Biochim Biophys Acta* 1847(11):1412–1423.
5. Mejia EM, Cole LK, Hatch GM (2014) Cardiolipin metabolism and the role it plays in heart failure and mitochondrial supercomplex formation. *Cardiovasc Hematol Disord Drug Targets* 14(2):98–106.
6. Rosca MG, et al. (2008) Cardiac mitochondria in heart failure: Decrease in respirasomes and oxidative phosphorylation. *Cardiovasc Res* 80(1):30–39.
7. Hesselink MK, Schrauwen-Hinderling V, Schrauwen P (2016) Skeletal muscle mitochondria as a target to prevent or treat type 2 diabetes mellitus. *Nat Rev Endocrinol* 12(11):633–645.
8. Simoes DC, et al. (2012) Glucocorticoid and estrogen receptors are reduced in mitochondria of lung epithelial cells in asthma. *PLoS One* 7(6):e39183.
9. Vyas S, Zaganjor E, Haigis MC (2016) Mitochondria and cancer. *Cell* 166(3):555–566.
10. Lane RK, Hilsabeck T, Rea SL (2015) The role of mitochondrial dysfunction in age-related diseases. *Biochim Biophys Acta* 1847(11):1387–1400.
11. Pagliarini DJ, et al. (2008) A mitochondrial protein compendium elucidates complex I disease biology. *Cell* 134(1):112–123.
12. Mootha VK, et al. (2003) Integrated analysis of protein composition, tissue diversity, and gene regulation in mouse mitochondria. *Cell* 115(5):629–640.
13. Schägger H, Pfeiffer K (2000) Supercomplexes in the respiratory chains of yeast and mammalian mitochondria. *EMBO J* 19(8):1777–1783.

14. Shinzawa-Itoh K, et al. (2016) Purification of active respiratory supercomplex from bovine heart mitochondria enables functional studies. *J Biol Chem* 291(8):4178–4184.
15. Schäfer E, Dencher NA, Vonck J, Parcej DN (2007) Three-dimensional structure of the respiratory chain supercomplex I1III2IV1 from bovine heart mitochondria. *Biochemistry* 46(44):12579–12585.
16. Kugelberg E (2016) Immunometabolism: Mitochondria adapt to bacteria. *Nat Rev Immunol* 16(8):464–465.
17. Lee CF, et al. (2016) Normalization of NAD+ redox balance as atherapy for heart failure. *Circulation* 134(12):883–894.
18. Papanicolaou KN, O'Rourke B, Foster DB (2014) Metabolism leaves its mark on the powerhouse: Recent progress in post-translational modifications of lysine in mitochondria. *Front Physiol* 5:301.
19. Giorgio V, et al. (2013) Dimers of mitochondrial ATP synthase form the permeability transition pore. *Proc Natl Acad Sci USA* 110(15):5887–5892.
20. Alavian KN, et al. (2014) An uncoupling channel within the c-subunit ring of the F1FO ATP synthase is the mitochondrial permeability transition pore. *Proc Natl Acad Sci USA* 111(29):10580–10585.
21. Letts JA, Fiedorczuk K, Sazanov LA (2016) The architecture of respiratory supercomplexes. *Nature* 537(7622):644–648.
22. Tang X, Munske GR, Siems WF, Bruce JE (2005) Mass spectrometry identifiable cross-linking strategy for studying protein-protein interactions. *Anal Chem* 77(1):311–318.
23. Liu F, Rijkers DT, Post H, Heck AJ (2015) Proteome-wide profiling of protein assemblies by cross-linking mass spectrometry. *Nat Methods* 12(12):1179–1184.
24. Weisbrod CR, et al. (2013) In vivo protein interaction network identified with a novel real-time cross-linked peptide identification strategy. *J Proteome Res* 12(4): 1569–1579.
25. Yu C, Kandur W, Kao A, Rychnovsky S, Huang L (2014) Developing new isotope-coded mass spectrometry-cleavable cross-linkers for elucidating protein structures. *Anal Chem* 86(4):2099–2106.
26. Tang X, Bruce JE (2010) A new cross-linking strategy: Protein interaction reporter (PIR) technology for protein-protein interaction studies. *Mol Biosyst* 6(6):939–947.
27. Wu X, et al. (2016) In vivo protein interaction network analysis reveals porin-localized antibiotic inactivation in Acinetobacter baumannii strain AB5075. *Nat Commun* 7:13414.
28. Hoopmann MR, et al. (2015) Kojak: Efficient analysis of chemically cross-linked protein complexes. *J Proteome Res* 14(5):2190–2198.
29. Schweppe DK, et al. (2016) Spectral library searching to identify cross-linked peptides. *J Proteome Res* 15(5):1725–1731.
30. Schweppe DK, Chavez JD, Bruce JE (2016) XLmap: An R package to visualize and score protein structure models based on sites of protein cross-linking. *Bioinformatics* 32(2): 306–308.
31. Fioramonte M, et al. (2012) Analysis of secondary structure in proteins by chemical cross-linking coupled to MS. *Proteomics* 12(17):2746–2752.
32. Stengel F, Aebersold R, Robinson CV (2012) Joining forces: Integrating proteomics and cross-linking with the mass spectrometry of intact complexes. *Mol Cell Proteomics* 11(3):R111.014027.
33. Navare AT, et al. (2015) Probing the protein interaction network of Pseudomonas aeruginosa cells by chemical cross-linking mass spectrometry. *Structure* 23(4):762–773.
34. Schweppe DK, et al. (2015) Host-microbe protein interactions during bacterial infection. *Chem Biol* 22(11):1521–1530.
35. Chavez JD, Schweppe DK, Eng JK, Bruce JE (2016) In vivo conformational dynamics of Hsp90 and its interactors. *Cell Chem Biol* 23(6):716–726.
36. Yang L, et al. (2012) In vivo application of photocleavable protein interaction reporter technology. *J Proteome Res* 11(2):1027–1041.
37. Zhang H, et al. (2009) Identification of protein-protein interactions and topologies in living cells with chemical cross-linking and mass spectrometry. *Mol Cell Proteomics* 8(3):409–420.
38. Zheng C, et al. (2011) Cross-linking measurements of in vivo protein complex topologies. *Mol Cell Proteomics* 10(10):M110.006841.
39. Chavez JD, Weisbrod CR, Zheng C, Eng JK, Bruce JE (2013) Protein interactions, post-translational modifications and topologies in human cells. *Mol Cell Proteomics* 12(5): 1451–1467.
40. Boehm EA, Jones BE, Radda GK, Veech RL, Clarke K (2001) Increased uncoupling proteins and decreased efficiency in palmitate-perfused hyperthyroid rat heart. *Am J Physiol Heart Circ Physiol* 280(3):H977–H983.
41. Karamanlidis G, et al. (2013) Mitochondrial complex I deficiency increases protein acetylation and accelerates heart failure. *Cell Metab* 18(2):239–250.
42. Brand MD, Nicholls DG (2011) Assessing mitochondrial dysfunction in cells. *Biochem J* 435(2):297–312.
43. Calvo SE, Clauser KR, Mootha VK (2016) MitoCarta2.0: An updated inventory of mammalian mitochondrial proteins. *Nucleic Acids Res* 44(D1):D1251–D1257.
44. Floyd BJ, et al. (2016) Mitochondrial protein interaction mapping identifies regulators of respiratory chain function. *Mol Cell* 63(4):621–632.
45. Nury H, et al. (2005) Structural basis for lipid-mediated interactions between mitochondrial ADP/ATP carrier monomers. *FEBS Lett* 579(27):6031–6036.
46. Huynen MA, Mühlmeister M, Gotthardt K, Guerrero-Castillo S, Brandt U (2016) Evolution and structural organization of the mitochondrial contact site (MICOS) complex and the mitochondrial intermembrane space bridging (MIB) complex. *Biochim Biophys Acta* 1863(1):91–101.
47. Harner M, et al. (2011) The mitochondrial contact site complex, a determinant of mitochondrial architecture. *EMBO J* 30(21):4356–4370.
48. Rabl R, et al. (2009) Formation of cristae and crista junctions in mitochondria depends on antagonism between Fcj1 and Su e/g. *J Cell Biol* 185(6):1047–1063.
49. Körner C, et al. (2012) The C-terminal domain of Fcj1 is required for formation of crista junctions and interacts with the TOB/SAM complex in mitochondria. *Mol Biol Cell* 23(11):2143–2155.
50. Friedman JR, Mourier A, Yamada J, McCaffery JM, Nunnari J (2015) MICOS coordinates with respiratory complexes and lipids to establish mitochondrial inner membrane architecture. *eLife* 4:4.
51. Kühlbrandt W (2015) Structure and function of mitochondrial membrane protein complexes. *BMC Biol* 13:89.
52. Chavez JD, et al. (2015) Quantitative interactome analysis reveals a chemoresistant edgotype. *Nat Commun* 6:7928.
53. Schweppe DK, et al. (2016) XLinkDB 2.0: Integrated, large-scale structural analysis of protein crosslinking data. *Bioinformatics* 32(17):2716–2718.
54. Lee J, et al. (2015) Organization of subunits in the membrane domain of the bovine F-ATPase revealed by covalent cross-linking. *J Biol Chem* 290(21):13308–13320.
55. Vinothkumar KR, Montgomery MG, Liu S, Walker JE (2016) Structure of the mitochondrial ATP synthase from Pichia angusta determined by electron cryo-microscopy. *Proc Natl Acad Sci USA* 113(45):12709–12714.
56. Bason JV, Montgomery MG, Leslie AG, Walker JE (2015) How release of phosphate from mammalian F1-ATPase generates a rotary substep. *Proc Natl Acad Sci USA* 112(19):6009–6014.
57. Zhu J, Vinothkumar KR, Hirst J (2016) Structure of mammalian respiratory complex I. *Nature* 536(7616):354–358.
58. Lange C, Hunte C (2002) Crystal structure of the yeast cytochrome bc1 complex with its bound substrate cytochrome c. *Proc Natl Acad Sci USA* 99(5):2800–2805.
59. Schneidman-Duhovny D, Inbar Y, Nussinov R, Wolfson HJ (2005) PatchDock and SymmDock: Servers for rigid and symmetric docking. *Nucleic Acids Res* 33(Web Server issue):W363–367.
60. Lapuente-Brun E, et al. (2013) Supercomplex assembly determines electron flux in the mitochondrial electron transport chain. *Science* 340(6140):1567–1570.
61. Biasutto L, Azzolini M, Szabò I, Zoratti M (2016) The mitochondrial permeability transition pore in AD 2016: An update. *Biochim Biophys Acta* 1863(10):2515–2530.
62. Dudkina NV, Sunderhaus S, Boekema EJ, Braun HP (2008) The higher level of organization of the oxidative phosphorylation system: Mitochondrial supercomplexes. *J Bioenerg Biomembr* 40(5):419–424.
63. Davies KM, et al. (2011) Macromolecular organization of ATP synthase and complex I in whole mitochondria. *Proc Natl Acad Sci USA* 108(34):14121–14126.
64. Davies KM, et al. (2014) Visualization of ATP synthase dimers in mitochondria by electron cryo-tomography. *J Vis Exp* 2014(91):e51228.
65. Bernardi P, Rasola A, Forte M, Lippe G (2015) The mitochondrial permeability transition pore: Channel formation by F-ATP synthase, integration in signal transduction, and role in pathophysiology. *Physiol Rev* 95(4):1111–1155.
66. Li B, et al. (2012) Inhibition of complex I regulates the mitochondrial permeability transition through a phosphate-sensitive inhibitory site masked by cyclophilin D. *Biochim Biophys Acta* 1817(9):1628–1634.
67. Fontaine E, Eriksson O, Ichas F, Bernardi P (1998) Regulation of the permeability transition pore in skeletal muscle mitochondria. Modulation by electron flow through the respiratory chain complex i. *J Biol Chem* 273(20):12662–12668.
68. Fontaine E, Bernardi P (1999) Progress on the mitochondrial permeability transition pore: Regulation by complex I and ubiquinone analogs. *J Bioenerg Biomembr* 31(4):335–345.
69. Porcelli AM, et al. (2009) Respiratory complex I dysfunction due to mitochondrial DNA mutations shifts the voltage threshold for opening of the permeability transition pore toward resting levels. *J Biol Chem* 284(4):2045–2052.
70. Surovtseva YV, Shadel GS (2013) Transcription-independent role for human mitochondrial RNA polymerase in mitochondrial ribosome biogenesis. *Nucleic Acids Res* 41(4):2479–2488.
71. Chavez JD, et al. (2016) A general method for targeted quantitative cross-linking mass spectrometry. *PLoS One* 11(12):e0167547.
72. Lam H, et al. (2007) Development and validation of a spectral library searching method for peptide identification from MS/MS. *Proteomics* 7(5):655–667.
73. Marcu R, Neeley CK, Karamanlidis G, Hawkins BJ (2012) Multi-parameter measurement of the permeability transition pore opening in isolated mouse heart mitochondria. *J Vis Exp* 2012(67):e4131.
74. Eng JK, Jahan TA, Hoopmann MR (2013) Comet: An open-source MS/MS sequence database search tool. *Proteomics* 13(1):22–24.
75. Keller A, Nesvizhskii AI, Kolker E, Aebersold R (2002) Empirical statistical model to estimate the accuracy of peptide identifications made by MS/MS and database search. *Anal Chem* 74(20):5383–5392.
76. Kelley LA, Mezulis S, Yates CM, Wass MN, Sternberg MJ (2015) The Phyre2 web portal for protein modeling, prediction and analysis. *Nat Protoc* 10(6):845–858.
77. Rose AS, Hildebrand PW (2015) NGL Viewer: A web application for molecular visualization. *Nucleic Acids Res* 43(W1):W576-9.
78. Roberts DL, Frerman FE, Kim JJ (1996) Three-dimensional structure of human electron transfer flavoprotein to 2.1-A resolution. *Proc Natl Acad Sci USA* 93(25):14355–14360.
79. Inaoka DK, et al. (2015) Structural insights into the molecular design of Flutolanil derivatives targeted for fumarate respiration of parasite mitochondria. *Int J Mol Sci* 16(7):15287–15308.
80. Suga M, et al. (2011) Distinguishing between Cl- and O2(2-) as the bridging element between Fe3+ and Cu2+ in resting-oxidized cytochrome c oxidase. *Acta Crystallogr D Biol Crystallogr* 67(Pt 8):742–744.